

Comparative study regarding the sputtering yield of nano-columnar tungsten surfaces under Ar⁺ irradiation

Alvaro Lopez-Cazalilla^{a,*}, Christian Cupak^{b,†}, Martina Fellingner^b, Fredric Granberg^a, Paul S. Szabo^c, Andreas Mutzke^d, Kai Nordlund^a, Friedrich Aumayr^b, and Raquel González-Arrabal^e

^aDepartment of Physics, P.O. Box 43, FI-00014 University of Helsinki, Finland

^bInstitute of Applied Physics, TU Wien, Fusion@ÖAW, Wiedner Hauptstraße 8-10/E134, 1040 Vienna, Austria

^cSpace Sciences Laboratory, University of California, 7 Gauss Way, Berkeley, CA 94720, United States

^dMax-Planck Institute for Plasma Physics, Wendelsteinstrasse 1, 17491 Greifswald, Germany

^eInstituto de Fusión Nuclear "Guillermo Velarde" and Departamento de Ingeniería Energética, ETSI de Industriales, Universidad Politécnica de Madrid, C/ José Gutiérrez Abascal, 2, E-28006 Madrid, Spain

*alvaro.lopezcazalilla@helsinki.fi

†cupak@iap.tuwien.ac.at

[†]Alvaro Lopez-Cazalilla and Christian Cupak contributed equally to this work.

ABSTRACT

Nanostructured tungsten has been proposed as a promising option for plasma facing materials in future fusion reactors, because compared to conventional tungsten it shows advantages such as a better radiation resistance and, in particular, a retardation of tungsten-fuzz growth. Besides these aspects, the sputtering yield of nanostructured tungsten under ion bombardment is of interest, since it would affect the atomic density of tungsten emitted into the fusion plasma, which leads to radiative heat losses. In this work, we present a multi-scale approach for investigating the sputtering yield of nano-columnar tungsten surfaces under 1 keV and 2 keV Ar⁺ irradiation. Our results cover experiments and also computational simulations, which operate either on the basis of the binary collision approximation and ray-tracing, or use a full molecular dynamics implementation. In our studied case, both computational approaches can predict the sputtering yield of nano-columnar tungsten surfaces very well. In comparison to flat W, we observed a much reduced dependence on the ion incidence angle, similar as reported for conventional rough surfaces in literature. However, an additional global reduction of the sputtering yield was identified, which can be attributed to geometrical redeposition effects between the separated nano-columns. These results support the applicability of nano-columnar tungsten as a first wall coating.

1 Introduction

Nuclear fusion has become one of the most promising concepts for future large-scale energy supply, due to the relatively high amount of energy released during the fusion process of deuterium and tritium. There are two main approaches to fusion energy: magnetic confinement fusion (MCF) and inertial confinement fusion (ICF). Both of them have recently achieved important milestones, supporting that the scientific community is on the right path to make fusion energy a reality^{1,2}. The largest-scale project to demonstrate the viability of MCF is the International Thermonuclear Experimental Reactor (ITER), now under construction in France and supported by a multinational consortium³⁻⁵. It has become one of the most encouraging paths to achieve the goal of establishing a reactor demonstrating net energy gain. Despite the achievements, there is still a number of challenges that need to be addressed prior up-scaling to a commercial facility. One of them is to select a durable material for the reactor first wall, which withstands the harsh environment (mainly high thermal load and high radiation flux) inside the reactor chamber⁶⁻⁹. In the case of MCF, the interaction of the plasma species (D, T, and He) with the first wall will result in detrimental effects such as blistering, He-induced W-fuzz formation, cracking, melting and erosion/sputtering. In the particular case of sputtering, wall released atoms will introduce radiative losses that affect the energy confinement efficiency of the plasma. This can result in a decrease of fusion reaction rates, which might be insufficient for maintaining net energy gain and can cause interruptions of the reactor operation. Therefore, it is important to know and to control the contribution of sputtering to wall erosion and plasma contamination.

So far, tungsten is assumed to be the best candidate as first wall material, especially in the divertor region, due to its high melting point, good thermal conductivity, low thermal expansion, significant strength at elevated temperatures and also its high sputtering

threshold energy^{10–13}. The latter property implies that the sputtering yield of tungsten is relatively low, making it a favourable option compared to other materials. However, during the plasma exposure of conventional coarse grained W (CGW) at reactor operation conditions, large He particle flux and high temperature can lead to the formation of W-fuzz, containing nanotendrils with typical dimensions of a few tens of nm in diameter and up to several microns in length^{14–16}. This can notably deteriorate the W properties, e.g., a reduction of thermal conductivity down to a fraction of $\frac{1}{100}$ was reported^{17,18}. The nano-structuring of W by largely increasing the grain boundary density, or by usage of engineered structures with large surface area (nanocolumns or nanofoams) results in higher radiation resistance^{19–28}. Qin *et al.* reported that the creation of nano-columnar tungsten surfaces (NC-W) reduced the development of W-fuzz during high-fluence helium plasma exposure²⁹, since helium could be quickly trapped and released along the channels between the nano-columns (NC). Also, a reduction of ion-induced erosion for similar columnar surface structures was reported in literature^{30,31}. While application of NC-W surfaces on the first wall of a future fusion device is therefore of interest, their sputtering characteristics, e.g. during ion bombardment with divertor-relevant seeding gas species like argon^{32,33}, need to be tested further.

Several techniques for measuring sputtering yields have been developed during the last decades. On the one hand, the sputtering yield can be evaluated as a function of the eroded thickness, e.g., as obtained from microscopy images after ion bombardment^{34,35}. On the other hand, the eroded volume of a material can be a basis for sputtering yield calculation, which is usually done in Focused Ion Beam (FIB) milling³⁶. However, these techniques require that the material surface is severely altered during the ion bombardment, which limits assessment of morphology-related effects on the sputtering yield. An alternative approach to circumvent this limitation is the use of a very sensitive quartz crystal microbalance (QCM)^{37–40}, where even very small mass losses can be determined *in-situ*. This technique was found to be very useful in situations where only low ion fluences are acceptable in sputtering yield experiments, to prevent dynamic changes of the surface morphology on rough samples⁴¹.

In addition to experimental techniques, computational methodologies have been developed during the last decades, which are able to describe the response of rough first wall materials during ion irradiation. Molecular dynamics (MD)⁴² simulations are an established technique which can consider interactions on the atomic level. MD simulations, reaching from irradiation energies between tens of eV up to tens of keV, have been carried out on different materials to understand the effect of various surface configurations on sputtering, but also the evolution of the surface morphology as a function of fluence^{43–47}. While the precise integration of atomic interaction in MD is a very fundamental approach, this, however, requires high computational resources and time.

Other prominent examples are numeric codes like TRI3DYN or SDTrimSP-3D, which employ the binary collision approximation (BCA)^{48,49}. These codes have been successfully applied in studies focusing on sputtering-induced morphology effects and achieved results consistent with experimental data^{50–54}. While these codes already allow to simulate topographies extending beyond 100 nm lateral size, consideration of larger surface inputs is still limited by computational resources. To liberate these constraints, ray-tracing approaches were developed, which enable computationally efficient extrapolation of BCA-based data to simulate even larger morphological structures^{41,55,56}.

In this work we have fabricated NC-W coatings with isolated NCs, similar to those previously reported to reduce W-fuzz formation, to experimentally determine their sputtering yield for both 1000 eV and 2000 eV Ar⁺ irradiation and as a function of the ion incidence angle. Using a QCM technique and a low-fluence approach, we aim to investigate the effects of the surface structure within a quasi-stationary surface approximation. We furthermore present results of a multi-scale and comparative numerical study, where BCA-based ray-tracing (SPRAY) and MD models were used to predict and explain the sputtering yields measured experimentally. The final aim is to characterize the applicability of NC-W as a first wall material from the perspective of sputtering by seeding gas ions.

2 Materials and Methods

2.1 Nano-column growth and characterization

Nano-columnar W coatings were deposited by DC magnetron sputtering from a pure W commercial target (99.95%), under oblique angle configuration (OAD). For this, the substrates were tilted with respect to their surface normal. The zenithal deposition angle (α) was 85°. Sputtering took place in a setup located at the IFN-GV at UPM, which is equipped with two magnetrons. The sputtering gas was pure argon (99.9999 %). Diverse set of coatings were deposited. Firstly, for morphological characterization, a bilayer consisting on 90 nm of Au and 650 nm of W was deposited on a single crystalline (100) Si to study the possible influence of the Au layer on the W morphology. Secondly, another sample was created, following the same deposition procedure but in the presence of an aluminum foil mask with a thickness of ~ 0.1 mm, to account for the possible influence of a mask. Thirdly, a W coating was deposited on a circular quartz resonator disk with a diameter of 14 mm, covered by 100 nm thin gold electrode layers on both sides of this disk (fabricated by the manufacturer KVG Quartz Crystal Technology GmbH, Germany). A similar aluminum foil mask was used to ensure that only the central region of the circular surface was covered, avoiding electrical shortcuts of the gold electrodes across the quartz disk edges. This substrate was chosen especially for sputtering yield experiments (more details can be found in section 2.2). In all

cases, the Ar pressure and flux were 8×10^{-3} mbar and 20 sccm, respectively. The plasma power and the target–substrate distance were 50 W and 8 cm, both for the Au and for the W deposition. Sputtering was performed at room temperature in all cases. The base pressure in the sputtering chamber was in the 10^{-7} mbar range.

The deposited NC-W morphology was characterized at first by high resolution field emission gun-scanning electron microscopy (FEG-SEM) using a JEOL JSM 7600F microscope. The peculiarities of the morphology (such as the angle of the NCs relative to the substrate surface normal, their diameter, or the surface area coverage of the NCs) were analysed by using the ImageJ⁵⁷ software. More than 200 nanocolumns were analysed in order to get reliable results. Cross-sectional and top-view SEM images of the deposited NC-W coatings are shown in Figure 1. The coating has a thickness of about 665 ± 8 nm and is made of isolated and elongated columns with a diameter of 50 ± 10 nm. In addition, a NC surface area coverage of $\sim 58\%$ was deduced. The NCs furthermore have conical or dome-shaped top structures (see Figure 1 (a) inset). Such a shape is very different from coatings deposited at $\alpha = 0^\circ$ ⁵⁸. This coating therefore exhibits a high roughness and porosity, while it also represents a very oriented type of nanostructure. Surprisingly, the columns grew perpendicular to the substrate surface normal, instead of having a tilt angle (β) of $\sim 65^\circ$. The latter has been observed for similar coatings deposited without a mask (for a first set of samples, not shown), which was explained by a self-shadowing effect⁵⁹. We attribute the origin of our perfectly perpendicular column orientation to the presence of the mask, which might have altered the particle flux during the deposition procedure. A top-view SEM image for the sputtered coatings is shown in Figure 1 (b). The small tilt of the NCs appearing in this image was caused by a SEM detector position off from the surface normal direction.

In addition to the SEM investigation, tapping-mode atomic force microscopy (AFM) was employed to characterize the surface morphology and roughness of the coatings on the quartz resonator disk. A Cypher S acquired from Asylum Research, Oxford Instruments (United Kingdom) was used to obtain images of 2×2 microns size and 1024×1024 px² resolution. We utilised the 240AC-NA AFM tips commercially available from the company OPUS for this study, and took 10 images at various lateral positions of the sample to obtain satisfying statistics. In Figure 2, a 3D visualisation of a selected AFM image is presented. In contrast to SEM, AFM has the advantage that quantitative data is available for each image. However, we observed a disadvantage caused by the finite width of the AFM tips. The narrow gaps between the columns observed in SEM (see Figure 1) were too tight for the AFM tips to reach down to the bottom surface of the substrate. This introduced a convolution between the actual surface topography with the tip geometry and had substantial effect on the resulting data. Nevertheless, we assume that at least the top structure of our sample was captured adequately. We therefore used these 10 AFM images as geometric input to one of our simulation methods, being the ray-tracing code SPRAY (see Section 2.3).

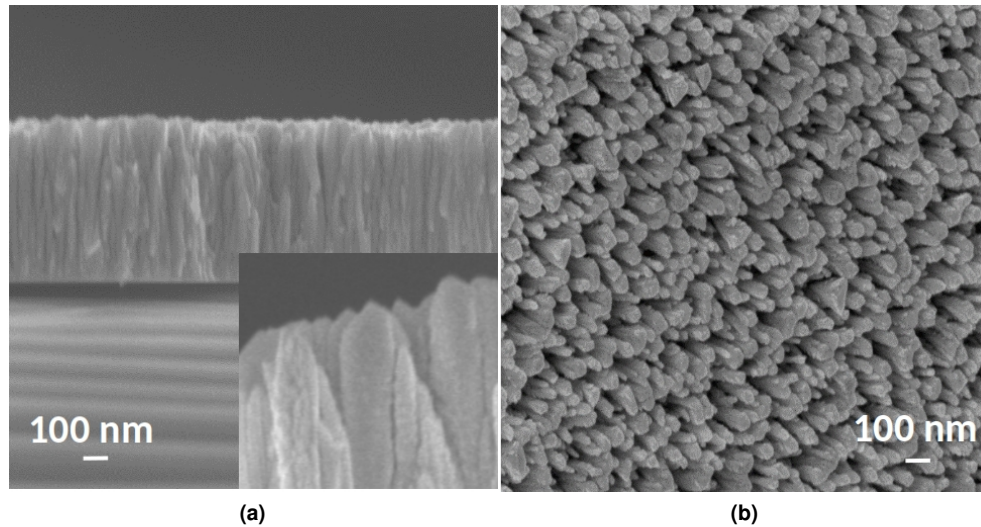


Figure 1. Cross-sectional (a) and top-view (b) SEM images of a NC-W coating deposited on a thin Au layer on a monocrystalline (100) Si substrate.

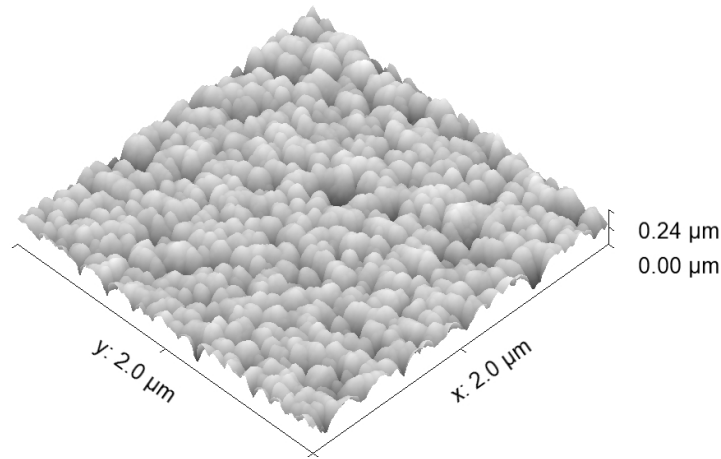


Figure 2. 3D visualisation of a selected AFM image measured on the NC-W coating, deposited on the quartz resonator disk. The visualisation was generated using the software Gwyddion⁶⁰.

2.2 Quartz Crystal Microbalance Experiment

A quartz crystal microbalance setup located at the TU Wien was used to experimentally determine sputtering yield values during ion bombardment in ultra high vacuum (UHV) conditions. It allows to record mass changes *in-situ* by measuring the frequency variations of a piezoelectric quartz resonator disk⁶¹. In this setup, a very high mass change sensitivity in the order of 10^{-4} W monolayers per second can be achieved, which is supported by using special SC-cut quartz resonator disks and dedicated electronics^{37,38,40}. For the experiments, one side of the QCM resonator disk was fully covered with the NC-W structures (as described in Section 2.1), which was then exposed to beams of 1000 eV or 2000 eV Ar^+ ions delivered from a mass-filtered SPECS IQE 12/38 ion source. Prior to each experiment, the sample was sputter-cleaned under normal ion incidence for a short time to reduce adsorbate contamination on the surface. The respective ion flux was determined by means of a Faraday cup before and after each measurement, ensuring steady ion irradiation. The ion incidence angle (θ) was varied between 0° and 70° in our experiments in discrete angular steps of 5° , by tilting the sample relative to the ion beam via a motor-controlled goniometer. Due to the high sensitivity of the QCM, low ion fluxes could be employed, which therefore resulted in very low total fluences and practically no surface modification. In total, the sample received a fluence of $7.4 \times 10^{19} \text{ Ar}\cdot\text{m}^{-2}$ at 1000 eV and $1.1 \times 10^{20} \text{ Ar}\cdot\text{m}^{-2}$ at 2000 eV. This low-fluence approach proved to be very robust for measuring static sputtering yields of W samples⁴¹. With information from both the mass loss and the ion flux, incidence-angle-dependent sputtering yields were calculated.

2.3 SPRAY simulations

Numerical simulations based on the binary collision approximation were performed by means of the ray-tracing code SPRAY⁴¹. SPRAY uses a repository data set containing sputtering yields, ion reflection coefficients and secondary particle trajectories (i.e., for sputtered target atoms and reflected ions) for a given ion-target combination. These can be obtained from BCA simulations like TRI3DYN⁴⁸ or SDTrimSP⁶². Furthermore, 3D topographies (e.g., from AFM images, or from computer generated structures) can be imported for SPRAY simulations, where static sputtering by ion impact is simulated using an efficient ray-tracing routine. This allows for consideration of geometric effects on sputtering, such as the variation of local ion incidence angles, surface shadowing and redeposition of sputtered particles or secondary sputtering by reflected ions. The SPRAY simulation settings and repository data sets were those previously used for Ar-W studies⁴¹. The main advantage of SPRAY in comparison to some other 3D BCA codes which also allow to handle complex surfaces^{48,53}, is its capability to run quick simulations of the sputtering yield as a function of ion incidence angle on common desktop PCs, while still enabling usage of large topography inputs without any limitations in size.

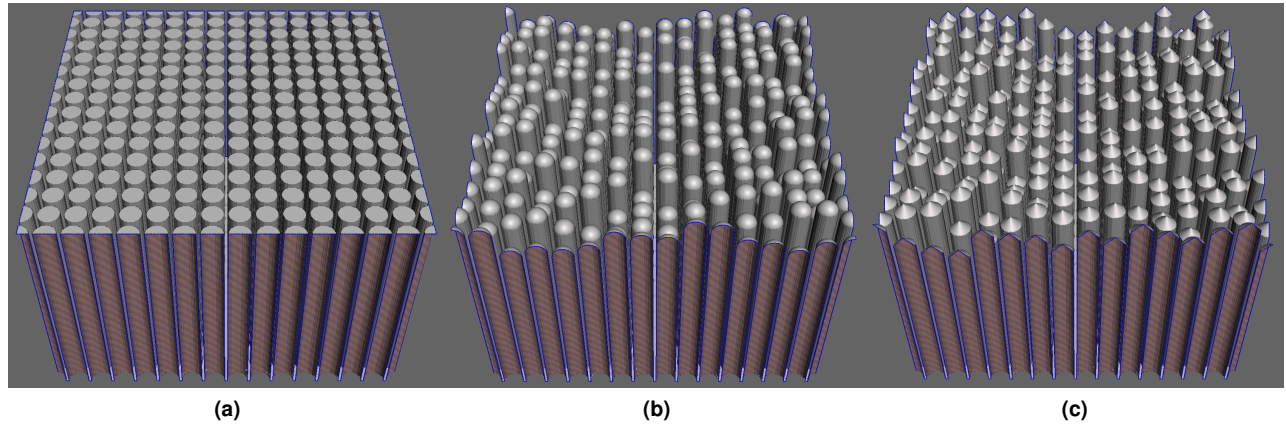


Figure 3. Visualisation of artificial computer-generated surface topographies used in the SPRAY simulations: (a) cylindrical nanocolumns with flat top (NC-cyl), (b) cylindrical nanocolumns with dome top and height variation (NC-dome), (c) cylindrical nanocolumns with conic top and height variation (NC-cone). For all cases, the column diameter was kept at 50 nm and the mean height at 550 nm. This visualisation was obtained using the software Meshmixer⁶³.

Besides the AFM images recorded from the experimental sample (see Section 2.1), also computer-generated surface topographies were used as input to SPRAY, which mimic the structures found by SEM (compare Figure 1). All generated structures are based on an arrangement with many cylindrical columns with a constant height of 550 nm and a diameter of 50 nm, in agreement with SEM data. Also the same NC surface area coverage ($\sim 58\%$, see Section 2.1) was considered. As a start, a rather simple geometry was considered with flat tops, labelled NC-cyl (Figure 3 (a)). Secondly, a dome-like top structure was added, accompanied with a small random height variation in the range of $\delta h = \pm 50$ nm for each NC, labelled by NC-dome (Figure 3 (b)). Finally, also a conical top structure with 45° inclination was considered, called NC-cone (Figure 3 (c)). The aim was to study the effect of different geometrical aspects on sputtering by starting from very simple structures, before more detailed features visible in the SEM images were added.

Since the lateral expansion of these artificially created surface topographies was already on the same scale as the average height of the columns, the incoming ions were only directed to the central 80% of the total lateral area. In doing so, boundary effects can be neglected in SPRAY simulations. In addition to the computer generated surface topographies shown above, also a perfectly flat surface was simulated for comparison. Since no effects like redeposition, shadowing or secondary sputtering by reflected ions can occur on a flat surface, the sputtering yield results were of course identical to the output of the BCA code SDTrimSP, which was used to generate the sputtering yield repository data.

2.4 Molecular Dynamics simulations

MD simulations were performed by using the PARCAS MD code⁴². The cells were built by setting periodic boundary conditions in x - and y -directions. The open surface, corresponding to the z -direction, was oriented as a (100) surface. The temperature of the simulations was kept at 300 K, dividing the cell in 3 different zones: a fixed layer composed by few atomic layers to prevent the cell from moving; on top of the fixed layer, some layers of atoms were kept in the NVT (canonical) ensemble, where the temperature was controlled by a Berendsen thermostat⁶⁴; and the rest of the cell followed a NVE (microcanonical) ensemble.

The details of the atomic interactions were as follows: the W-W interactions were described via a potential developed by Marinica et al.⁶⁵ with the corrections by Sand et al.⁶⁶ and the Ar-W and Ar-Ar interactions were defined by the DMol potential⁶⁷. Besides, electronic stopping power was considered for all atoms with kinetic energies larger than 10 eV. The incoming ion was always initiated 10 Å over the highest point of the cell. Different irradiation angles (θ) from normal (0°) to grazing incidence (80°) were investigated. The azimuthal angle (ϕ) was always fixed at 45° and the position of the incoming ion was set to impact in the center of the cell. However, in order to get statistically meaningful results, the impact point on the cell was randomized by arbitrarily shifting the cell in the x - and y - directions through the periodic boundaries. The selection of $\phi = 45^\circ$ was motivated by the randomness of the orientation with respect to the ion beam.

A sequential-impacts scheme^{68,69} was used, considering 2000 random impacts in the same cell in order to follow the evolution of the surface up to a certain fluence. A single-crystalline W BCC box, oriented as a (100) flat surface, was created and used as a

reference to perform the sequential impact simulations in the NC structures.

Two cylindrical W nano-columns (NC) from a (100) surface (see Figure 4), were resulting in a flat top (NC-cyl) and in a dome top (NC-dome) NC, which contained 60 932 and 58 405 atoms, respectively. The geometric parameters are $[a, L, h] = [78, 112, 113] \text{ \AA}$. The size of the NCs is larger than the SDTrimSP⁶² predicted mean implantation depth at normal incidence for Ar^+ in W (16 \AA and 24 \AA , respectively for 1000 eV and 2000 eV). Considering these two different cells, we can compare with the SPRAY simulations using similar input structures (see Figure 3).

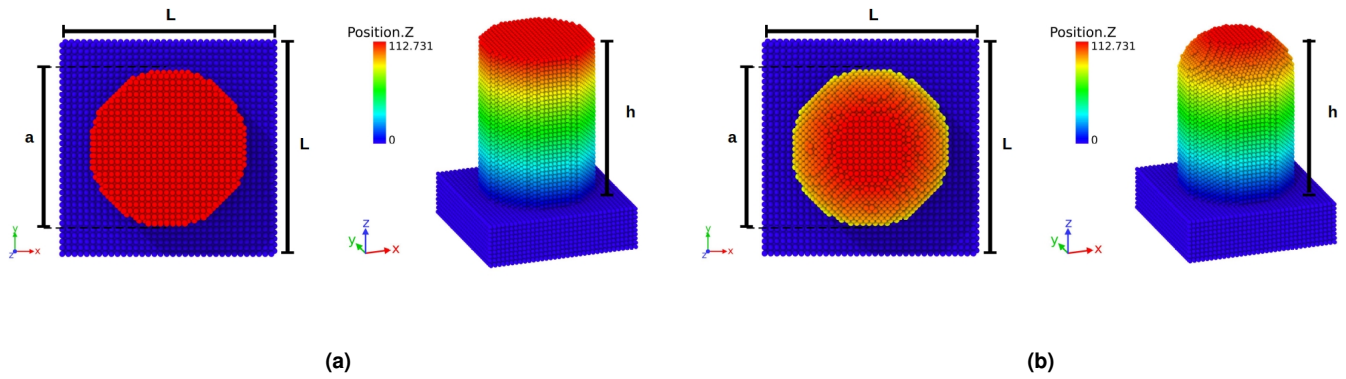


Figure 4. Configuration of the W NCs: (a) flat top (NC-cyl) and (b) dome top (NC-dome). The atoms are colored according to their height in \AA .

3 Results

3.1 QCM experiments

Figure 5 shows the experimental sputtering yield as a function of the irradiation angle θ , for 1000 eV and 2000 eV Ar^+ irradiation. To detect eventual dynamic changes during the experiment, two measurement runs (labelled I and II) were carried out. In the first measurement runs (indicated by I), the incidence angle was increased step-wise from 0° to 70° , in steps of 5° , while in the second runs (II) the sequence of incidence angles was reversed. We observe that the sputtering yield dependence on the incidence angle follows a similar trend for both energies. At 1000 eV energy, the sputtering yield remains almost constant at a value of $0.56 \pm 0.04 \text{ W/Ar}$ in the range from 0° to 45° , before it moderately increases to obtain a maximum of $0.79 \pm 0.06 \text{ W/Ar}$ at the technical range limit at 70° . Compared to the 1000 eV case, an enhancement of the sputtering yield by an almost constant factor is seen for the 2000 eV case over all irradiation angles, starting from $0.96 \pm 0.07 \text{ W/Ar}$ at 0° towards $1.26 \pm 0.10 \text{ W/Ar}$ at 70° . The results between the individual measurement runs are in excellent agreement and therefore no dynamic changes are expected.

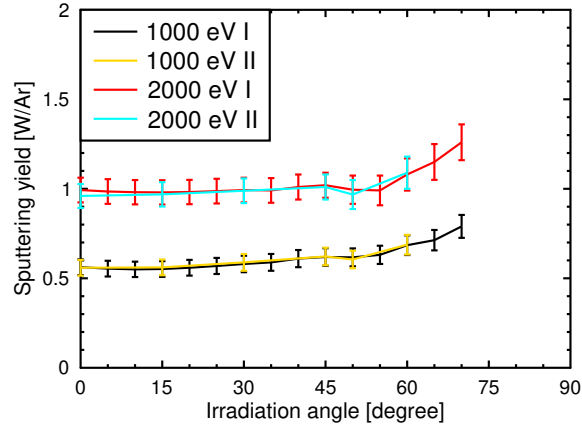


Figure 5. Sputtering yields as a function of the ion incidence angle, measured by the QCM for 1000 eV and 2000 eV Ar^+ ions on NC-W coatings. I and II stand for two individual experimental runs performed at each energy. The second run (II) is done in reverse direction from 60° to 0° for reproducibility.

3.2 SPRAY results

In Figure 6, simulation results obtained by SPRAY using the different surface input options (perfectly flat, AFM, NC-cyl, NC-cone and NC-dome) are presented. To mimic the experiments, the sputtering yield was simulated for both 1000 eV and 2000 eV Ar^+ irradiation (Figure 6 (a) and (b), respectively) as a function of the ion irradiation angle θ .

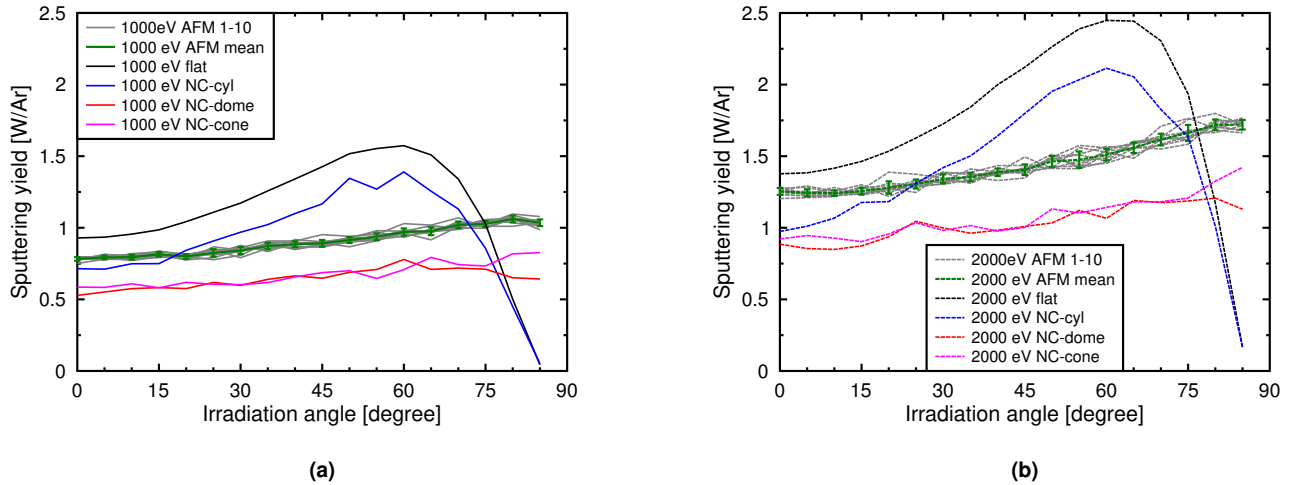


Figure 6. SPRAY simulated W sputtering yields as a function of the Ar^+ irradiation angle for a perfectly flat (black line), NC-cyl (blue line) NC-dome (red line) and NC-cone (purple line) surface and for both energy cases (a) 1000 eV and (b) 2000 eV. The AFM results are based on the input of 10 AFM images. Both the trends based on individual AFM images (grey lines) and the mean trend of all AFM images (green line) are shown (standard deviation of the mean is plotted as error bar).

From the qualitative point of view, the usage of perfectly flat and NC-cyl surfaces led to a similar sputtering yield trend. At irradiation angles lower than $\sim 60^\circ$, the sputtering yield increases with rising irradiation angle up to a maximum at 60° . At larger

angles, the sputtering yield strongly decreases with rising irradiation angle, becoming almost 0 W/Ar at 85° . From the quantitative point of view, by comparing the data calculated for these two input surfaces, we observe that at irradiation angles lower than 60° the sputtering yield values for the NC-cyl surface are lower than those for the flat surface. This difference diminishes beyond the maxima, where both data become more and more similar and start to overlap when the ion incidence angle approaches 90° . Increasing the irradiation energy from 1000 eV (Figure 6 (a)) to 2000 eV (Figure 6 (b)) does not significantly change the qualitative dependence of the sputtering yield on the irradiation angle, but only increases the sputtering yield values and slightly shifts the maximum towards higher irradiation angles for both cases.

The qualitative dependence of the sputtering yield on the irradiation angle for the AFM, NC-dome and NC-cone surface inputs shows very similar trends. For all these input options, a moderate but continuous increase in the sputtering yield is observed for increasing irradiation angles. These results are different from those previously discussed for the flat and NC-cyl surfaces. From the quantitative point of view, the sputtering yield values calculated for the NC-dome and NC-cone surfaces are very similar and only a small deviation is observed at large irradiation angles. In contrast, the obtained values by using AFM images are generally higher than those for the NC-dome and NC-cone surfaces. In addition to the mean sputtering yield data based on all AFM images, also the individual data for each image are shown in Figures 6 (a) and (b) for comparison, while the individual trends do not scatter dramatically. Increasing the irradiation energy (from 1000 eV to 2000 eV) does, again, not significantly change the qualitative dependence of the sputtering yield on irradiation angle, but only increases the absolute values.

3.3 Molecular Dynamics

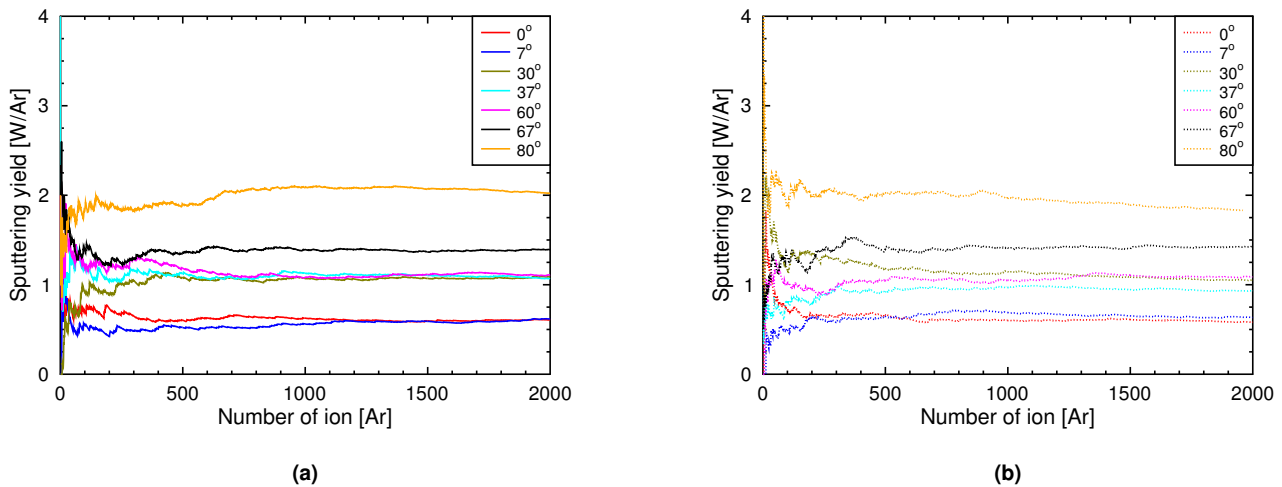


Figure 7. Evolution of W sputtering yield as a function of the fluence for (a) 2000 eV Ar^+ on NC-cyl and (b) 2000 eV Ar^+ on NC-dome cell for the different irradiation angles.

Figure 7 (a) shows the sputtering yield as a function of the number of ion impacts on the surface for the NC-cyl cell at 2000 eV for different irradiation angles. In the beginning of the simulations, a large variation of the sputtering yield is observed. However, this process becomes constant just about 800 impacts. This effect is also observed for the irradiation at 1000 eV. For this reason, we consider the average sputtering yield after 2000 impacts (which corresponds to a fluence of $1.59 \times 10^{19} \text{Ar} \cdot \text{m}^{-2}$), where all the curves have clearly reached a plateau. In Figure 7 (b), the evolution of the sputtering yield as a function of the fluence for the NC-dome cell can be seen. We notice that the results for all angles tend to fluctuate slightly less for the case of the NC-dome cell, where stable values can be obtained at lower fluences (after about 600 impacts), compared to the flat NC.

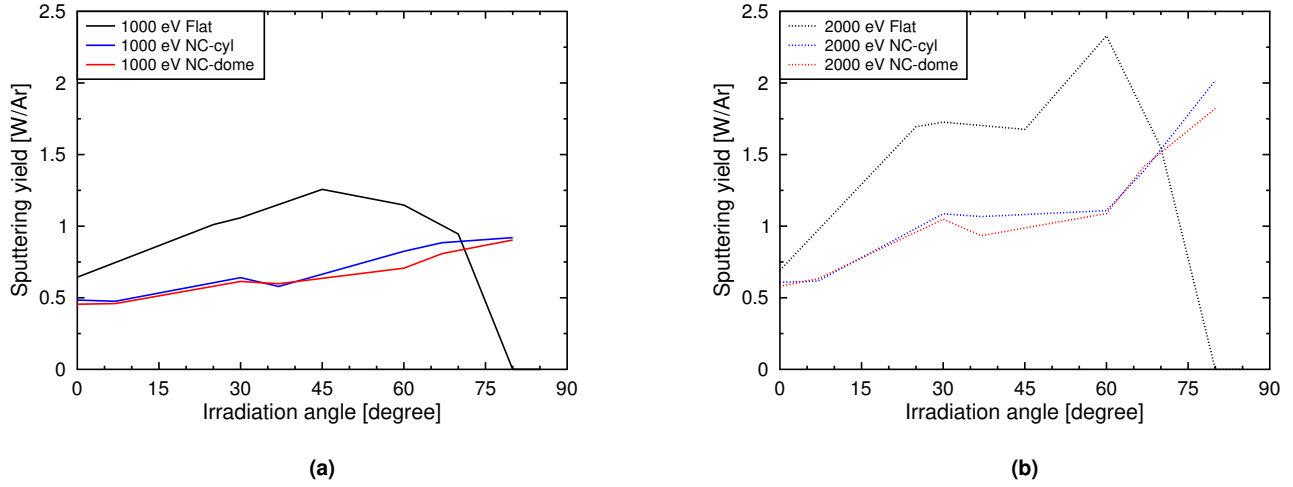


Figure 8. MD simulated W sputtering yields for (a) 1000 eV and (b) 2000 eV Ar^+ ion energy, for the (100) flat surface, the NC-cyl structure and the NC-dome structure, as a function of the irradiation angle, all averaged after 2000 impacts.

In Figure 8, we compare the results obtained for the cells shown in Figure 4 as well as for the flat (100) surface at 1000 eV and 2000 eV Ar^+ irradiation. For the flat surface, we observe that at large irradiation angles ($\theta > 70^\circ$), the sputtering yield drops to zero, due to the declining energy deposition at such inclinations. A similar trend was also observed in Figure 6 for the SPRAY simulations for both simulated energies. Moreover, we notice a displacement of the maximum value in the 2000 eV case, which can now be found at 60° (Figure 8 (b)), instead of 45° in the 1000 eV irradiation (Figure 8 (a)). On the other hand, for the NC cases we perceive how the sputtering increases until it reaches a maximum at the largest irradiation angle. This effect is induced by the NC, which breaks the flatness of the sample and, therefore, the atoms are sputtered more easily at large incoming angles, especially at 2000 eV (Figure 8(b)). Moreover, as the fluence increases, the local incidence angle on the top of the NC changes, contributing to the increase of sputtering yield at grazing incidence (see Figure 9).

When considering the results obtained for the NCs, we see that the sputtering yields are rather similar for NC-cyl and NC-dome at 1000 eV (Figure 8 (a)). However, the NC-cyl provides a slightly higher value in the range from about 40° to grazing incidence, where they are almost identical. When considering the 2000 eV case (Figure 8 (b)), we observe magnified results compared to the lower energy, and see how the NC-cyl provides a slightly higher sputtering yield for $\theta > 37^\circ$, obtaining the highest discrepancy at 80° .

Generally, we observe that the different tops induce only small variations on the results depending on the irradiation angle. At 1000 eV, the NC-dome only moderately decreases the sputtering yield between $40^\circ < \theta < 80^\circ$, while at 2000 eV, the NC-dome cell suppresses the erosion at grazing incidence slightly more ($\theta > 67^\circ$).

In general, we observed that for $\theta < 60^\circ$ ion incidence the sputtering yield is higher for the flat surface (black lines in Figure 8) than for any of the NC cells, i.e., the NCs are acting as a suppressor of the sputtering yield at small irradiation angles. However, this effect inverts when the irradiation angle further increases, i.e., it becomes easier to remove atoms from the NC surface. To investigate this effect, we further analyzed the final frames for those irradiation angles, where the sputtering yield curve reached its minimum and maximum (i.e., 0° and 80°).

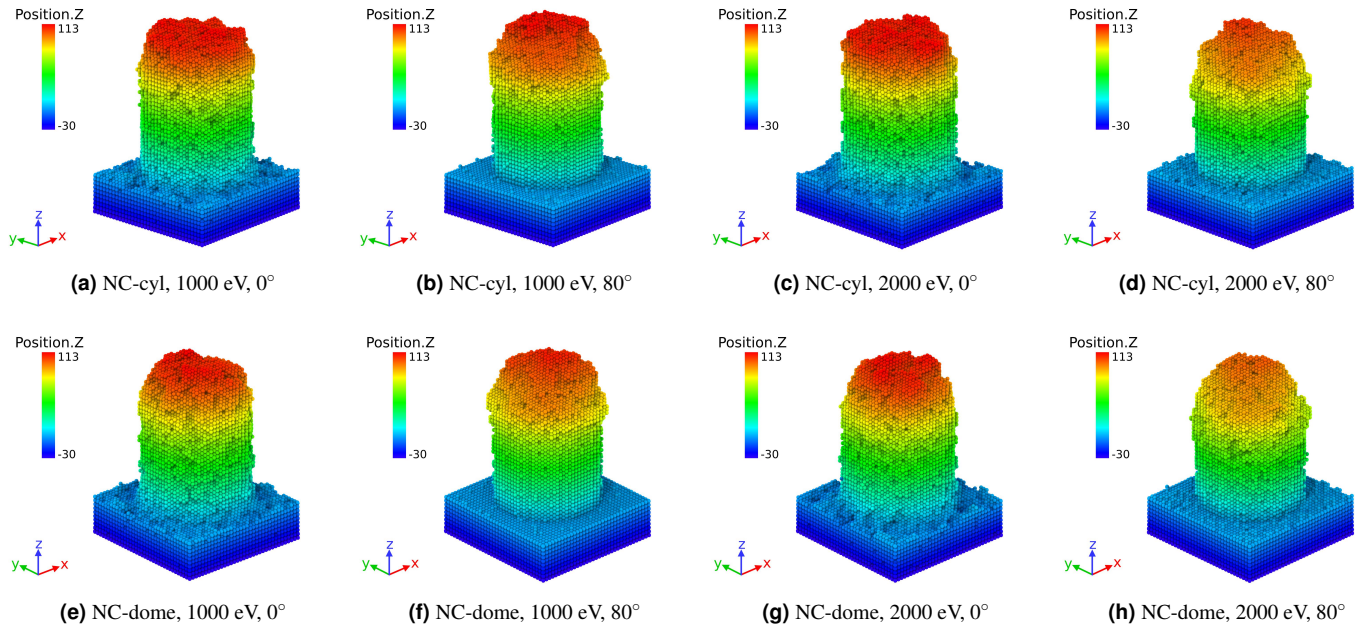
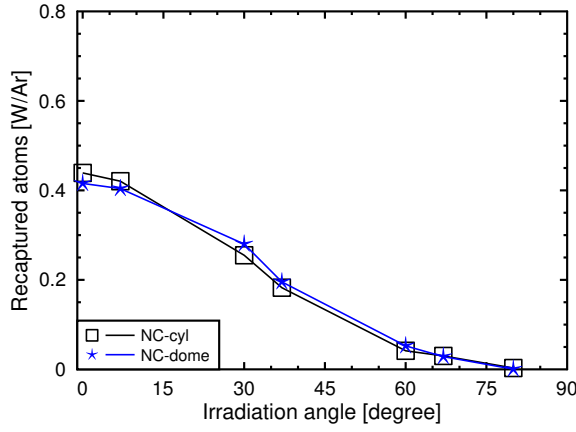


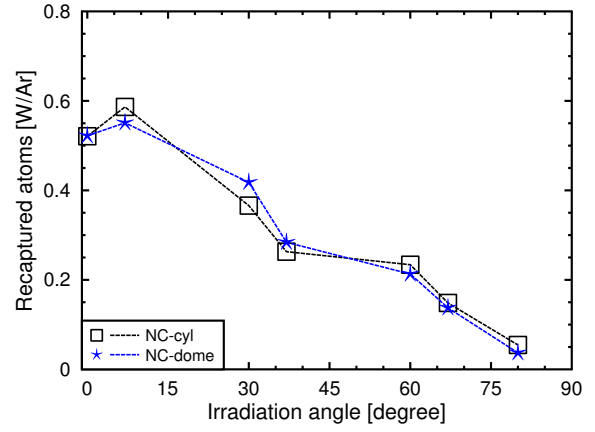
Figure 9. Final configuration (after 2000 impacts) of the NC-cyl (a-d) and NC-dome cells (e-h) under 1000 eV and 2000 eV Ar^+ irradiation at 0° and 80° irradiation angle, respectively. The atoms are colored according to their height in Å.

Figure 9 shows the configuration of the NC-cyl (a-d) and NC-dome (e-h) cells after 2000 Ar^+ impacts at different energies and irradiation angles. Several differences can be noted between the individual cases. At 1000 eV, the NC-cyl cell at normal incidence (Figure 9(a)) has lost its flatness of the bottom due to erosion. This is a result of W atoms being sputtered from the bottom and recaptured on the NC sidewalls, decreasing the eventual sputtering yield. The top of the NC also increased its roughness, however, not as much as in the 80° case (Figure 9 (b)), where most of the damage and sputtering is focused on the NC top. At 2000 eV, the NC-cyl cells (Figures 9 (c) and (d)) show a magnified effect with respect to the 1000 eV case. Especially at 80° (Figure 9 (d)), we observe how the region of the NC facing the incoming ions is slightly more eroded, resulting in a small height reduction of the NC in comparison to the 0° case. This is a product of the incoming irradiation which mainly focuses on the top of the NC at grazing inclination. The change on the top can be noticed from the color scale: the top of NC appears now rather orange, corresponding to the small height loss. For the NC-dome configuration (Figures 9 (e-h)), we see that they follow a similar evolution compared to the NC-cyl cell, leading to a rather similar outcome. Nevertheless, we observe differences in the initial stages of the irradiation (see Figure 7), where the curved top provides smaller fluctuations and rather sooner plateaus in the evolution of the sputtering yield.

One feature which can be further investigated is the sputtering of the initially flat bottom layer in the NC cells. In Figure 9 we see how at normal incidence the bottom of the cell is considerably more damaged than at 80° , where basically no erosion occurred. In MD, we can follow an atom that was originally part of the bottom surface outside of the NC contour, but is finally found to stick on the sidewall of the NC. In this case, it is considered as recaptured in the following. The MD simulations allow to label atoms which satisfy this criterion and therefore enables assessment of the number of recaptured bottom surface atoms per incoming Ar^+ ion.



(a) 1000 eV



(b) 2000 eV

Figure 10. Number of recaptured bottom surface atoms per incident Ar^+ , as a function of the irradiation angle for (a) 1000 eV and (b) 2000 eV on NC-cyl and NC-dome cells.

In Figure 10 (a) we observe how the number of recaptured atoms per incident Ar^+ decreases as a function of the irradiation angle for the 1000 eV case. Due to geometric considerations, at normal incidence the number of ions that arrive to the bottom surface is larger than at grazing incidence, hence, there are more opportunities to remove atoms from the bottom and redeposit them on the NC sidewalls, as can be seen for instance in Figures 9 (a) and (b). This results in a maximum value close to 0° , and a drastic decline as the irradiation angle increases. Consequently, the probability of direct interaction of Ar^+ ions with the bottom surface also decreases as the irradiation angle increases. This demonstrates how well the presence of NC structures act as an additional source for the sputtering yield reduction.

For the 2000 eV irradiation, while being in very good agreement with the 1000 eV case, the individual trends for the NC-cyl and NC-dome cases slightly differ more (see Figure 10 (b)). The generally higher values in the 2000 eV case originate from the fact, that principally more atoms are sputtered than in the 1000 eV scenario.

4 Discussion

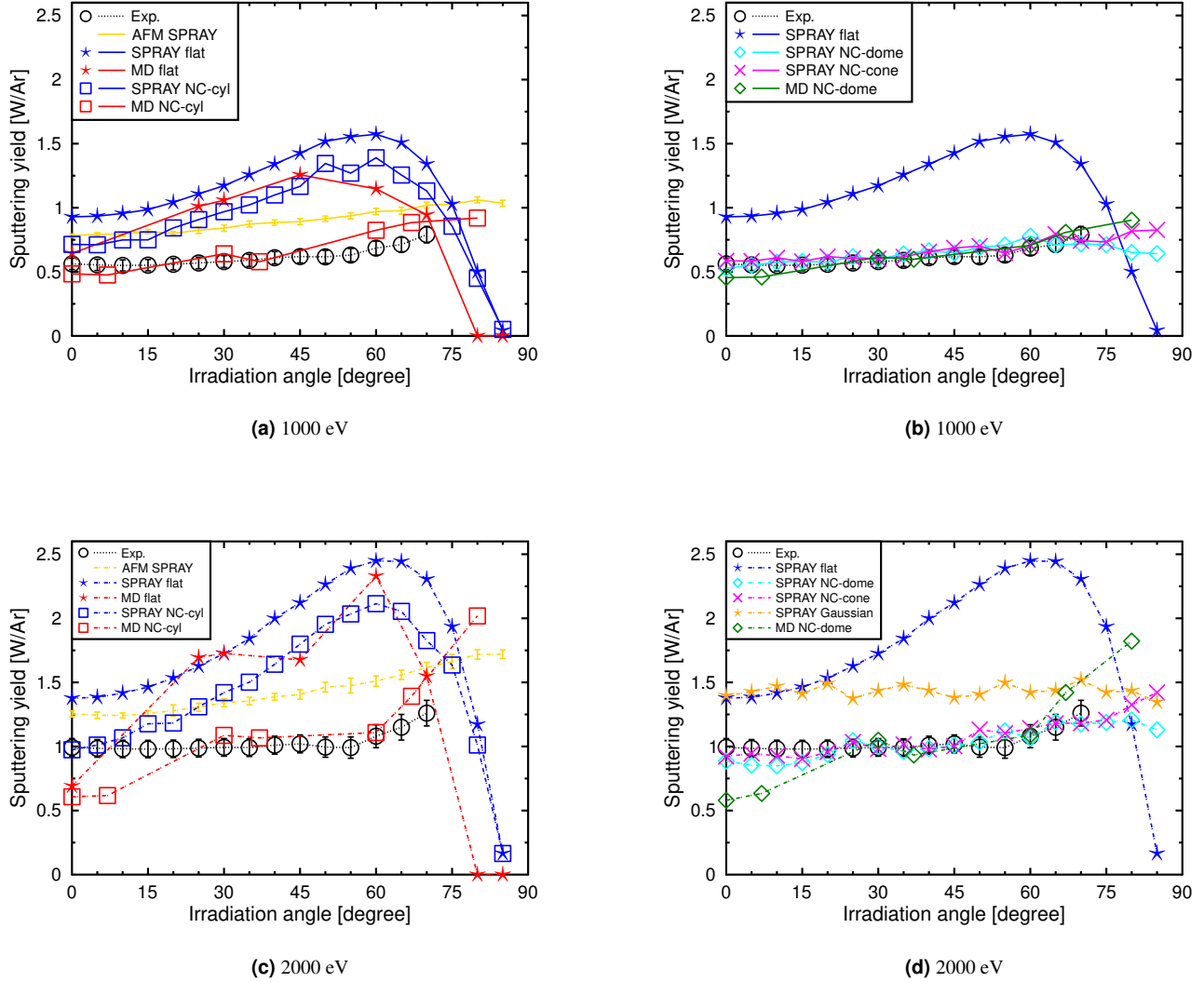


Figure 11. Comparative plot of W sputtering yields as a function of Ar^+ ion incidence angle from QCM experiments, SPRAY and PARCAS MD simulations. The 1000 eV cases are grouped in subfigures (a) and (b), while the 2000 eV cases can be studied in subfigures (c) and (d). The data set SPRAY Gaussian (orange) in subfigure (d) is taken from a study on 2000 eV Ar^+ sputtering of conventionally rough W surfaces with Gaussian distributed height values⁴¹.

A collection of data shown in the previous sections is combined in Figure 11, in order to enable a comparison between the experimental results from QCM and computationally obtained results from SPRAY and MD. The Figures 11 (a) and (b) correspond to the results for 1000 eV ion energy, while the Figures 11 (c) and (d) contain 2000 eV results.

By focusing first on the simulated data only, we observe that SPRAY and MD data tendencies agree well when using NC-dome surfaces, but differ when simulating NC-cyl surfaces, even though a similar input structure was used for both. This is because SPRAY uses a static geometry in which the initial flat top surface for the NC-cyl surface is always preserved, whereas the MD simulations led to a quick modification of the flat top surface towards a rounded top structure (see Figure 9). These results are a first indication about

the strong influence of the top structure of a surface on the sputtering yield. Indeed, the sputtering yield dependence on irradiation angle calculated by SPRAY for the NC-cyl case resembles the tendency obtained for perfectly flat surfaces, especially at grazing ion incidence. This is related to projection effects, since in contrast to cases with a certain top roughness, the flat tops of these NCs appear comparable to a completely flat surface when viewed from a grazing angle. Additionally, the larger the irradiation angle, the lower the probability that an incoming ion can be transmitted deep into the narrow channels becomes.

As a next step, the computational results are compared in more detail with the experimental data for the 1000 eV case. In both Figures 11 (a) and (b) we observe that the experimental sputtering yield values and the dependence on the irradiation angle are lower than those simulated for perfectly flat surfaces, both with SPRAY and MD. These results agree quite well with those previously reported in literature for conventional rough W surfaces⁴¹ as well as for other metals with similar surfaces^{70,71}. A mix of local incidence angle variation, redeposition and secondary sputtering can cause the angular dependence of the sputtering yield to change dramatically. Moreover, a general reduction of the sputtering yield compared to a flat surface was obtained for most irradiation angles, except for the region beyond 75°.

A general reduction, even though not as strong as for the experimental data, is also found for the SPRAY NC-cyl case. This reduction is attributed to redeposition of sputtered atoms in the depths of the narrow channels between the NCs. It can be assumed that the strength of reduction is connected to the NC surface area coverage and the height of NCs.

The SPRAY simulations based on the AFM images (AFM SPRAY) also resulted in a sputtering yield reduction. Still, the experimental values were found to be lower also compared to this case. However, the global trend of the sputtering yield over increasing incidence angle is in relatively good agreement with the experimental data. This supports that the global sputtering yield tendency is strongly dependent on the top structure of a surface. A combination of AFM images with SPRAY was therefore found to be useful also for investigation of these challenging surfaces. The remaining constant offset between the experimental and simulated AFM SPRAY data can be attributed to the convolution effects found during the AFM investigation (see Section 2.1). This convolution led to an underestimation of the depth and shape of the narrow channels which separate the NCs, resulting in less redeposition events in the simulation. Therefore, the agreement between experiments and SPRAY simulations using AFM inputs decreases. This differs from a previous study focusing on more moderately rough W surfaces with Gaussian distributed height values⁴¹.

For the results of the SPRAY simulated NC-dome and NC-cone structures, which are shown in Figure 11 (b) for the 1000 eV case, a synergy of the former described geometric effects led to an even stronger global reduction of the sputtering yield, while also the angular dependence is flattened. This led to an outstanding agreement with the experimental data. Besides the implementation of separated NCs, the addition of a rough top structure was definitely relevant in these cases. Only at very grazing ion incidence angles beyond 75°, the data sets show a moderate divergence. However, since the technically available incidence angles in our experiments were limited to 70°, no judgement can be made which surface structure performs better in this region. It has to be mentioned, that these inputs were created *a priori* to mimic the geometric aspects of the morphology characterized in the SEM analysis. Since SPRAY is furthermore a purely geometric simulation code, this good agreement supports the assumption that geometric effects are the dominant cause for the experimentally observed change of sputtering yield tendency in our studied case.

Considering the MD results using the round-shaped top input (MD NC-dome), also a good agreement between experiments and simulated data is obtained, as well as for the flat top case MD NC-cyl. However, compared to the NC-cyl case, the NC-dome surface led to a slightly lower sputtering yield at grazing ion incidence ($\theta > 60^\circ$). This effect is related to the fact that the local incidence angle of ions arriving at the cell differs from the global one. This decreases the sputtering yield, since the cell has a less pronounced border on the top in the case of the curved top (see Figure 4). In other words, the larger amount of atoms weakly bound to others on top of the NC-cyl cell is important to understand the rapid fluctuation of the sputtering yield, at least during the initial stage of the simulations (see Figure 7 (a)).

By consideration of the results in Figure 9, which show that the NC-dome input structure did not severely change during the dynamic MD simulation, we conclude that the geometric effects discussed before were also dominant for the results of the sputtering yield simulations in MD. It has to be mentioned, that the NC diameter considered in the MD simulations was about 10 times smaller than found by SEM, due to computational resource constraints. Taking into account that the NC height was even reduced by a factor of about 50, it can be assumed that the effect of redeposition within the narrow channels between NCs is saturating relatively fast with increasing NC height. In addition, the angular dependence of the number of recaptured bottom surface atoms (see Figure 10), which decreases as the irradiation angle increases, follows an opposite trend to the sputtering yield (Figure 11, MD NC-cyl and MD NC-dome). This shows the probability of the ion to interact with the bottom surface. The recapturing contribution definitely dominates the redeposition at around normal incidence, where the ions can reach the bottom surface directly. However, as the irradiation angle increases, the recapturing of sputtered atoms from the NC sidewalls on the bottom surface will start to be considerable, causing additional redeposition. Then, at grazing incidence, the recapturing on the NC sidewalls vanishes.

In Figures 11 (c) and (d), all results for the 2000 eV case are presented. As expected, globally higher sputtering yield values were

found. For this energy regime and ion-target combination, the effect of sputtering yield enhancement for increasing kinetic energy is known from literature, and can be theoretically described since decades⁷². Qualitatively, the same conclusions can be still drawn as for the 1000 eV scenario, while it was recognised that for the MD NC-cyl case a stronger scatter is present in the data. Even so, the overall trend follows an increase of the sputtering yield as the irradiation angle rises, predicting a quantitatively good agreement with the experiments for $30^\circ \leq \theta \leq 67^\circ$ also in the MD NC-cyl and MD NC-dome cases.

To further highlight the individual contributions of roughness effects, also a SPRAY data set from literature is added to Figure 11 (d). This data (orange stars) corresponds to sputtering yields of a rough W surface with Gaussian distributed height values for the same 2000 eV Ar⁺ irradiation conditions⁴¹. A mean surface inclination angle δ_m of about 45° was determined for this surface. While this is a statistical quantity for characterizing a conventional rough surface, it corresponds well to the constant inclination angle of the top cones applied in the NC-cone surface of this study. It can be seen that this surface causes a complete reduction of the sputtering yield dependency on the incidence angle towards a constant trend. These sputtering yields resemble the value for a flat W surface under 0° ion incidence. In comparison to the SPRAY NC-cone and NC-cyl data, it becomes visible that the top roughness of the NCs is the main responsible for the reduction of incidence angle dependence, while the inclusion of NCs decreases the sputtering yield further by an almost constant value for most ion incidence angles. A part of this effect was also quantitatively demonstrated by MD simulations, as can be seen in Figure 10 where the recapture effect of sputtered atoms from the bottom surface towards the NC sidewalls is shown. The results at 2000 eV also show that our presented description, focusing mostly on geometric effects, remains applicable for the higher energy case, where even larger ion ranges are achieved.

Summarizing, we were able to show that geometry was the origin of most sputtering effects observed experimentally. Considering the large difference in length scales between SPRAY and MD, we found very good agreement both in trends and absolute values of the simulated sputtering yields. It has to be mentioned, that the NCs considered in MD appear shorter than in SEM or SPRAY cases, by comparing the relevant aspect ratios between NC diameter and height. Nevertheless, the good agreement of our results indicates that much shorter NCs could have been used to achieve similar effects on the sputtering yields. From the sputtering point of view, it can be therefore assumed that a NC growth height of just 80 nm would be sufficient for a first wall coating, if the other geometric parameters remain unchanged. In addition, stationary conditions like maintained in our experiments can only provide a picture of the current geometric effects on sputtering, but for the first walls of a nuclear fusion device, much higher ion fluences will probably lead to surface modification. Also, problems related to thermo-mechanical properties, similarly to those found for W-fuzz, can be relevant for the NC-W structures as well. While being of major interest for future investigations, these points are beyond the scope of this work.

5 Conclusions

In this study, we investigated the effects of a highly corrugated, but also highly oriented type of roughness on sputtering. We used a W sample with a surface covered by isolated and vertically oriented nano-columns, having diameters of 50 nm and several 100 nm height, similar to those previously reported to reduce W-fuzz formation. We first employed a QCM technique to experimentally obtain the sputtering yield of this nano-columnar W coating under Ar⁺ ion irradiation, as a function of the ion incidence angle and for both 1000 eV and 2000 eV energy. Steady-state surface conditions were ensured by using only very low ion fluences. Compared to perfectly flat surfaces, a main result is that the sputtering yield was reduced globally, but also the angular dependence was drastically flattened. We furthermore used two different computational methods, SPRAY and MD, which differ substantially in terms of their implemented physical models, to predict sputtering yields and compare them with the experimental results. SEM images were used as inspiration for geometric remodelling in computer-generated topographies, which enabled SPRAY to achieve excellent reproduction of the experimental results. We therefore conclude that geometry effects are the dominant cause for the strong effects on the sputtering yield. In this context, the top roughness on the nano-columns was found to be responsible for the reduction of the sputtering yield dependence on the irradiation angle, while an additional global reduction was caused by the separated columnar structure, leading to enhanced redeposition. Our findings were also supported by the results of MD simulations, which show very good agreement with both experiments and SPRAY, regardless of the spatial scale differences. Based on the MD simulation results, it is suggested that a similar behavior may be also found for substantially shorter NCs as for those studied experimentally in this work. Additionally, it was shown by the dynamic MD simulations that for a similar ion fluence as applied during the experiments, the overall NC shape remained relatively stable. In this context, the ability of dynamic simulations in MD is a clear advantage in comparison to static calculations. Finally, from the aspect of sputtering, the NC-W coatings studied in this work exhibit better properties than smooth CGW for the first walls of future nuclear fusion devices, since the sputtering by seeding gas ions like Ar⁺ can be reduced significantly.

Acknowledgements

This work has been carried out within the framework of the EUROfusion Consortium, funded by the European Union via the Euratom Research and Training Programme (Grant Agreement No 101052200 — EUROfusion). Views and opinions expressed are however those of the author(s) only and do not necessarily reflect those of the European Union or the European Commission. Neither the European Union nor the European Commission can be held responsible for them. Computer time granted by the IT Center for Science – CSC – Finland and the Finnish Grid and Cloud Infrastructure (persistent identifier urn:nbn:fi:research-infras-2016072533) is gratefully acknowledged. The research leading to these results has partially received funding from the Spanish MICINN Project (PID2019-105325RB-C32), the Techno-Fusion Project (S2018/EMT-4437) and *Convenio Plurianual con la Universidad Politécnica de Madrid en la línea de actuación Programa de Excelencia para el Profesorado Universitario of the CAM (Comunidad Autónoma Madrid)* Financial support has also been provided by KKKÖ (commission for the coordination of fusion research in Austria at the Austrian Academy of Sciences - ÖAW). We also highly acknowledge continuous support with BCA codes by Prof. Wolfhard Möller, HZDR, Germany.

Author contributions statement

A.L.-C. and C.C. wrote the manuscript, A.L.-C., F.G and K.N. conceived the MD simulations, A.L.-C. performed the MD simulations, A.L.-C. and F.G. analyzed the MD results. C.C., M.F., P.S.S. and F.A. conceived the QCM experiments and SPRAY simulations. C.C. and M.F performed the QCM experiments and SPRAY simulations. C.C analyzed the QCM and SPRAY results. R.G.-A. prepared and characterized the samples for the experiments. A.M provided access to BCA codes. All authors reviewed the manuscript.

References

1. European researchers achieve fusion energy record. <https://www.euro-fusion.org/news/2022/european-researchers-achieve-fusion-energy-record/>. Accessed: 2022-3-3.
2. Kritcher A.L *et al.* Design of inertial fusion implosions reaching the burning plasma regime. *Nat. Phys.* (2022).
3. ITER Physics Basis Editors *et al.* ITER Physics Basis, I. *Nucl. Fusion* **39**, 2137 (1999).
4. K. Ikeda. Progress in the ITER physics basis. *Nucl. Fusion* **47**, 12 (2007).
5. Wesson, J. Tokamaks, Second Oxford Engineering Series. *Clarendon Press. Oxf.* (1997).
6. Ueda, Y. *et al.* Research status and issues of tungsten plasma facing materials for ITER and beyond. *Fusion Eng. Des.* **89**, 901–906 (2014).
7. Knaster, J. *et al.* Materials research for fusion. *Nat. Phys.* **12**, 424–434 (2016).
8. Budaev, V. Results of high heat flux tests of tungsten divertor targets under plasma heat loads expected in ITER and tokamaks (review). *Phys. At. Nucl.* **79**, 1137–1162 (2016).
9. Alvarez, J. *et al.* Materials Research for HiPER Laser Fusion Facilities: Chamber Wall, Structural Material and Final Optics. *Fusion Sci. Technol.* **60**, 565–569 (2011).
10. Barabash, V. *et al.* Armour Materials for the ITER Plasma Facing Components. *Phys. Scr.* **1999**, T81 (1999).
11. Nygren, R. *et al.* Making tungsten work. *J. Nucl. Mater.* **417**, 451–456 (2011).
12. Alvarez, J. *et al.* The role of spatial and temporal radiation deposition in inertial fusion chambers: the case of HiPER. *Nucl. Fusion* **51**, 053019 (2011).
13. Kaufmann M. *et al.* Tungsten as first wall material in fusion devices. *Fusion Eng. Des.* **82**, 521–527 (2007).
14. Baldwin, M.J. *et al.* Helium induced nanoscopic morphology on tungsten under fusion relevant plasma conditions. *Nucl. Fusion* **48**, 035001 (2008).
15. Wang, K. *et al.* Morphologies of tungsten nanotendrils grown under helium exposure. *Sci. Rep.* **7**, 42315 (2017).
16. Kajita, S. *et al.* Tungsten fuzz: Deposition effects and influence to fusion devices. *Nucl. Mater. Energy* **25**, 100828 (2020).
17. Gerasimov, D.N. *et al.* The heat exchange reduction of tungsten "fuzz" surface irradiated with helium plasma in the PLM device. *J. Phys.: Conf. Ser.* **1370**, 012047 (2019).
18. Kajita, S. *et al.* Measurement of heat diffusion across fuzzy tungsten layer. *Results Phys.* **6**, 877–878 (2016).

19. Beyerlein, I. *et al.* Radiation damage tolerant nanomaterials. *Mater. Today* **16**, 443–449 (2013).
20. Rivera, A. *et al.* Effect of ion flux on helium retention in helium-irradiated tungsten. *Nucl. Instrum. Methods Phys. Res. B* **303**, 81–83 (2013).
21. Stelmakh, V. *et al.* Evolution of sputtered tungsten coatings at high temperature. *J. Vac. Sci. & Technol. A* **31**, 061505 (2013).
22. Martinez, J. *et al.* Thermal stability of the grain structure in the W-2V and W-2V-0.5Y₂O₃ alloys produced by hot isostatic pressing. *Proc. 27th Symp. Fusion Technol. SOFT-27 Liege Belg.* **88**, 2636–2640 (2013).
23. Gonzalez-Arrabal, R. *et al.* Hydrogen accumulation in nanostructured as compared to the coarse-grained tungsten. *J. Nucl. Mater.* **453**, 287–295 (2014).
24. Andrievski, R. Review of thermal stability of nanomaterials. *J. Mater. Sci.* **49**, 1449–1460 (2014).
25. Liu, W. *et al.* Irradiation induced microstructure evolution in nanostructured materials: A review. *Materials* **9**, 105 (2016).
26. Valles, G. *et al.* Influence of grain boundaries on the radiation-induced defects and hydrogen in nanostructured and coarse-grained tungsten. *Acta Materialia* **122**, 277–286 (2017).
27. Panizo-Laiz, M. *et al.* Experimental and computational studies of the influence of grain boundaries and temperature on the radiation-induced damage and hydrogen behavior in tungsten. *Nucl. Fusion* **59**, 086055 (2019).
28. Fernández-Pello, D. *et al.* Coexistence of a self-interstitial atom with light impurities in a tungsten grain boundary. *J. Nucl. Mater.* **560**, 153481 (2022).
29. Qin, W. *et al.* Nanochannel structures in W enhance radiation tolerance. *Acta Materialia* **153**, 147–155 (2018).
30. Ghoniem, N.M. *et al.* Sputtering of molybdenum and tungsten nano rods and nodules irradiated with 150 eV argon ions. *Appl. Surf. Sci.* **331**, 299–308 (2015).
31. Matthes, C.S.R. *et al.* Fluence-dependent sputtering yield of micro-architected materials. *Appl. Surf. Sci.* **407**, 223–235 (2017).
32. Kallenbach, A. *et al.* Impurity seeding for tokamak power exhaust: from present devices via ITER to DEMO. *Plasma Phys. Control. Fusion* **55**, 124041 (2013).
33. Urano, H. *et al.* Roles of argon seeding in energy confinement and pedestal structure in JT-60U. *Nucl. Fusion* **55**, 033010 (2015).
34. Ecke, G. *et al.* The estimation of sputtering yields for SiC and Si. *Nucl. Instrum. Methods Phys. Res. B* **196**, 39–50 (2002).
35. Kotis, L. *et al.* Determination of relative sputtering yield of Cr/Si. *Vacuum* **82**, 178–181 (2007).
36. Stark, Y. *et al.* Sputter yields of single- and polycrystalline metals for application in focused ion beam technology. *J. Appl. Phys.* **105**, 013542 (2009).
37. Hayderer, G. *et al.* A highly sensitive quartz-crystal microbalance for sputtering investigations in slow ion–surface collisions. *Rev. Sci. Instruments* **70**, 3696 (1999).
38. Golczewski, A. *et al.* A quartz-crystal-microbalance technique to investigate ion-induced erosion of fusion relevant surfaces. *Nucl. Instrum. Methods Phys. Res. B* **267**, 695–699 (2009).
39. Kolasinski, R.D. *et al.* Carbon sputtering yield measurements at grazing incidence. *Appl. Surf. Sci.* **254**, 2506–2515 (2008).
40. Stadlmayr, R. *et al.* A high temperature dual-mode quartz crystal microbalance technique for erosion and thermal desorption spectroscopy measurements. *Rev. Sci. Instruments* **91**, 125104 (2020).
41. Cupak, C. *et al.* Sputter yields of rough surfaces: Importance of the mean surface inclination angle from nano- to microscopic rough regimes. *Appl. Surf. Sci.* **570**, 151204 (2021).
42. Nordlund, K. Molecular dynamics simulation of ion ranges in the 1–100 keV energy range. *Comp. Mater. Sci.* **3**, 448–456 (1995).
43. Lopez-Cazalilla, A. *et al.* Simulation of atomic redistribution effects in a-Si under ion irradiation. *Nucl. Instrum. Methods Phys. Res. B* **414**, 133–140 (2018).
44. Lopez-Cazalilla, A. *et al.* Pattern formation on ion-irradiated Si surface at energies where sputtering is negligible. *J. Appl. Phys.* **123**, 235108 (2018).
45. Jussila, J. *et al.* Effect of random surface orientation on W sputtering yields. *Nucl. Mater. Energy* **17**, 113–122 (2018).
46. Granberg, F. *et al.* Low energy sputtering of Mo surfaces. *J. Nucl. Mater.* **539**, 152274 (2020).

47. Hodille, E.A. *et al.* Sputtering of beryllium oxide by deuterium at various temperatures simulated with molecular dynamics. *Phys. Scr.* **2020**, 014024 (2020).
48. Möller, W. TRI3DYN – Collisional computer simulation of the dynamic evolution of 3-dimensional nanostructures under ion irradiation. *Nucl. Instrum. Methods Phys. Res. B* **322**, 23–33 (2014).
49. Von Toussaint, U. *et al.* Sputtering of rough surfaces: a 3D simulation study. *Phys. Scripta* **T170**, 014056 (2017).
50. Stadlmayr, R. *et al.* Fluence dependent changes of surface morphology and sputtering yield of iron: Comparison of experiments with SDTrimSP-2D. *Nucl. Instrum. Methods Phys. Res. B* **430**, 42–46 (2018).
51. Stadlmayr, R. *et al.* Sputtering of nanostructured tungsten and comparison to modelling with TRI3DYN. *J. Nucl. Mater.* **532**, 152019 (2020).
52. Stadlmayr, R. *et al.* Erosion of iron-tungsten model films by deuterium ion irradiation: a benchmark for TRI3DYN. *Phys. Scripta* **T171**, 014021 (2020).
53. Arredondo, R. *et al.* Angle-dependent sputter yield measurements of keV D ions on W and Fe and comparison with SDTrimSP and SDTrimSP-3D. *Nucl. Mater. Energy* **18**, 72–76 (2019).
54. Nakamura, H. *et al.* Sputtering yield of noble gas irradiation onto tungsten surface. *J. Adv. Simul. Sci. Eng.* **3**, 165–172 (2017).
55. Kim, H.-B. *et al.* Full three-dimensional simulation of focused ion beam micro/nanofabrication. *Nanotechnology* **18**, 245303 (2007).
56. Nadvornick, W. *et al.* A linked-scale coupled model of mass erosion and redistribution in plasma-exposed micro-foam surfaces. *J. Nucl. Mater.* **553**, 153010 (2021).
57. Schneider, C.A. *et al.* Nih image to imagej: 25 years of image analysis. *Nat. Methods* **9**, 671–675 (2012).
58. Gordillo, N. *et al.* Morphological and microstructural characterization of nanostructured pure α -phase W coatings on a wide thickness range. *Appl. Surf. Sci.* **316**, 1–8 (2014).
59. Barranco, A. *et al.* Perspectives on oblique angle deposition of thin films: From fundamentals to devices. *Prog. Mater. Sci.* **76**, 59–153 (2016).
60. Nečas, D. *et al.* Gwyddion: an open-source software for SPM data analysis. *Cent. Eur. J. Phys.* **10**, 181–188 (2011).
61. Sauerbrey, G. Verwendung von Schwingquarzen zur Wägung dünner Schichten und zur Mikrowägung. *Zeitschrift fuer Physik* **155**, 206–222 (1959).
62. Mutzke, A. *et al.* SDTrimSP Version 6.00. *IPP-Report Max-Planck-Institute fuer Plasmaphysik* **2** (2019).
63. Autodesk Inc. Meshmixer. *Off. Website* URL: <https://meshmixer.com/> (accessed February 7th, 2022).
64. Berendsen, H.J.C. *et al.* Molecular dynamics with coupling to an external bath. *J. Chem. Phys.* **81**, 3684–3690 (1984).
65. Marinica, M. *et al.* Interatomic potentials for modelling radiation defects and dislocations in tungsten. *J. Phys.* **25**, 395502 (2013).
66. Sand, A.E. *et al.* Non-equilibrium properties of interatomic potentials in cascade simulations in tungsten. *J. Nucl. Mater.* **470**, 119–127 (2016).
67. Nordlund, K. *et al.* Repulsive interatomic potentials calculated using hartree-fock and density-functional theory methods. *Nucl. Instrum. Methods Phys. Res. B* **132**, 45–54 (1997).
68. Lopez-Cazalilla, A. *et al.* Modeling of high-fluence irradiation of amorphous Si and crystalline Al by linearly focused Ar ions. *J. Phys. Condens. Matter* **31**, 075302 (2018).
69. Lopez-Cazalilla, A. *et al.* Direct observation of ion-induced self-organization and ripple propagation processes in atomistic simulations. *Mater. Res. Lett.* **8**, 110–116 (2020).
70. Eksaeva, A. *et al.* Surface roughness effect on Mo physical sputtering and re-deposition in the linear plasma device PSI-2 predicted by ERO2.0. *Nucl. Mater. Energy* **19**, 13–18 (2019).
71. Chang, F.J. *et al.* Rough-surface effect on sputtering of Cr bombarded by low-energy He plasma. *Nucl. Mater. Energy* **29**, 101077 (2021).
72. Eckstein, W. Sputtering Yields. In: *Sputtering by Particle Bombardment. Topics in Applied Physics. Springer, Berlin, Heidelberg.* **110** (2007).